PCCP

PAPER

View Article Online
View Journal | View Issue



Cite this: *Phys. Chem. Chem. Phys.*, 2018, **20**, 29472

# Phase transition and superconductivity in $ReS_2$, $ReSe_2$ and $ReTe_2$

Jurong Zhang,[a] Ermiao Sun,[a] Xiaolei Feng,[ab] Hanyu Liu,[a] Simon A. T. Redfern,[b] V. Kanchana,[c] Guangtao Liu*[ad] and Hongbo Wang*[a]

Received 23rd August 2018,
Accepted 6th November 2018

DOI: 10.1039/c8cp05333b

rsc.li/pccp

Transition metal dichalcogenides have attracted significant attention due to both fundamental interest and their potential applications. Here, we have systematically explored the crystal structures of $ReX_2$ (X = S, Se, and Te) over the pressure range of 0–300 GPa, employing swarm-intelligence-based structure prediction methodology. Several new structures are found to be stable at high pressures. The calculated enthalpy of formation suggested that all predicted high-pressure structures are stable against decomposition into elemental end-members. Moreover, we found that the simulated X-ray diffraction patterns of $ReSe_2$ are in good agreement with experimental data. Pressure-induced metallization of $ReX_2$ has been revealed from the analysis of its electronic structure. Our electron–phonon coupling calculations indicate $ReSe_2$ and $ReTe_2$ are superconducting phases at high pressures.

## Introduction

Transition-metal dichalcogenides ($TMX_2$) (TM = W, Mo, Re, Rb, Tc, *etc.*; X = S, Se, and Te) are mostly layered materials, in which TM atomic layers are sandwiched between two chalcogen atom layers, forming an X–M–X sandwiched structure.[1–5] The X–M–X trilayers then stack together *via* weak van der Waals (vdW) interactions, resulting in different phases of transition-metal dichalcogenides (TMDs) such as 1T, 1T′, $2H_c$, $2H_a$ and 3R.[4,6] Therefore, the bulk phases of TMDs exhibit a broad spectrum of electronic behaviors ranging from insulators to metals or even superconductors.[4,6,7]

Recently, $ReX_2$ (X = S, Se, and Te) has attracted significant attention, with reports of photoluminescent properties, catalytic behavior and promising solar-cell applications.[8–11] $ReX_2$ compounds are semiconducting layered transition metal dichalcogenides that exhibit a low-symmetry stable distorted 3R CdCl structure ($P\bar{1}$) under ambient conditions,[12–14] in which Re atoms are surrounded by six chalcogen atoms in a trigonal prism coordination under ambient conditions. The effects of pressure in reducing inter-atomic distances and modifying crystal structures are well known, thus pressure may provide a route to engineer and improve the physical and chemical properties of materials.[15] An early experimental study on $ReS_2$ revealed a high-pressure phase at ~11.3 GPa.[16] Recently, Zhou *et al.*[17] reported that the distorted-3R ($P\bar{1}$) phase, stable at 0 GPa, will transform to a distorted-1T phase, also with $P\bar{1}$ symmetry, at 3 GPa, and then to a non-layered $I4_1/amd$ structure at 90 GPa, which is stable up to at least 200 GPa. Remarkably, the nonlayered $I4_1/amd$ structure of $ReS_2$ shows superconductivity (with $T_c \approx 2$ K) below 100 GPa. The selenide equivalent, $ReSe_2$, was found to undergo a phase transition at ~10 GPa using angular-dispersive X-ray diffraction (ADXRD)[18] with the appearance of a new peak; however, the crystal structure and properties of $ReSe_2$ of the new phase have not been defined. A similar phase transition in $ReSe_2$ was also found at ~7 GPa by Naumov, as confirmed by Raman spectroscopy which showed the redistribution of Raman peak intensities and a discontinuity in the pressure dependence of the vibration frequencies at this pressure.[19] The two experimental works on $ReSe_2$ therefore support each other. For the telluride, $ReTe_2$, the high-pressure behavior is still completely unknown.

In this work, we have explored the high-pressure behaviors of $ReX_2$ over the pressure range of 0–300 GPa. By using the particle swarm optimization technique,[20] in combination with *ab initio* calculations, we have discovered a number of proposed high-pressure candidate structures and analyzed their electronic properties, which reveal pressure-induced metallization in this family of solids.

## Computational details

We have studied the structures of $ReX_2$ using the particle swarm optimization technique implemented in the CALYPSO

[a] *State Key Laboratory of Superhard Materials & Innovation Center for Computational Physics Method and Software, College of Physics, Jilin University, Changchun 130012, China. E-mail: whb2477@jlu.edu.cn; Web: 07455@163.com*
[b] *Department of Earth Sciences, University of Cambridge, Downing Street, Cambridge CB2 3EQ, UK*
[c] *Department of Physics, Indian Institute of Technology Hyderabad, Kandi, 502285 Sangareddy, Telangana, India*
[d] *National Key Laboratory of Shock Wave and Detonation Physics, Institute of Fluid Physics, China Academy of Engineering Physics, Mianyang 621900, China*

code.[20,21] This has been proved to be a reliable method for the successful predictions of high pressure structures for a wide variety of systems.[22,23] We research the structures of $ReX_2$ (X = S, Se, and Te) systems with unit cell sizes ranging from 1 to 4 formulas per simulation cell at 0, 50, 100, 150, 200, 250, and 300 GPa. Each generation contained 30 structures, and the first generation was produced randomly with symmetry constraint. The 60% lowest-enthalpy structures of each generation were used to produce the structures in the next generation by the local Particle Swarm Optimization (PSO) technique, and the remaining 40% structures were randomly generated within symmetry constraint to enhance the structural diversity. Total-energy calculations and geometrical optimization for these structures were performed in the framework of density functional theory within the Perdew–Burke–Ernzerhof[24] parametrization of the generalized gradient approximation[25] as implemented using the VASP code.[26] In order to obtain accurate results, the vdW interaction was taken into consideration. The interaction among the electrons and ions was simulated by the all-electron projector augmented-wave (PAW) method[27] and the $5s^25p^66s^25d^5$, $3s^23p^4$, $4s^24p^4$, and $5s^25p^4$ electrons were set as valence electrons for Re, S, Se and Te atoms, respectively. We chose a cutoff energy of 500 eV as the plane-wave kinetic energy cutoff and used Monkhorst–Pack[28] $k$ meshes with a grid spacing of $2\pi \times 0.03$ Å$^{-1}$. The dynamical stability of the crystal structures was calculated using a finite displacement as implemented in the PHONOPY code.[29] Superconducting properties were calculated within the framework of linear response theory using the Quantum-ESPRESSO code.[30] The plane-wave pseudopotential method of ultrasoft Vanderbilt pseudopotentials within density functional perturbation theory was used to calculate the EPC (electron–phonon coupling). We choose 50 Ry for the kinetic energy cutoff of the plane-wave basis after testing for convergence. The $k$-space and $q$-point integrations over the Brillouin zone (BZ) were performed on a $28 \times 28 \times 6$ grid and a $14 \times 14 \times 3$ grid of the $P6_3/mmc$ phase of $ReSe_2$, a $20 \times 20 \times 6$ grid and a $10 \times 10 \times 3$ grid of the $I4/mmm$ phase of $ReSe_2$ and a $24 \times 24 \times 6$ grid and a $12 \times 12 \times 3$ grid of the $I4/mmm$ phase of $ReTe_2$, respectively. The crystal-orbital Hamilton population was calculated using the LOBSTER code[31] for the binding analysis of $ReX_2$ (X = S, Se, and Te). The EPC spectral function is expressed by the phonon linewidth $\gamma_{\vec{q}j}$ arising from electron–phonon scattering,[32–34]

$$\alpha^2F(\omega) = \frac{1}{2\pi N_f}\sum_{\vec{q}j}\frac{\gamma_{\vec{q}j}}{\omega_{\vec{q}j}}\delta(\hbar\omega - \hbar\omega_{\vec{q}j})w(\vec{q}) \quad (1.1)$$

where $N_f$ is the electronic density of states/atom and spin at the Fermi level. The linewidth of the phonon mode $j$ at the wave

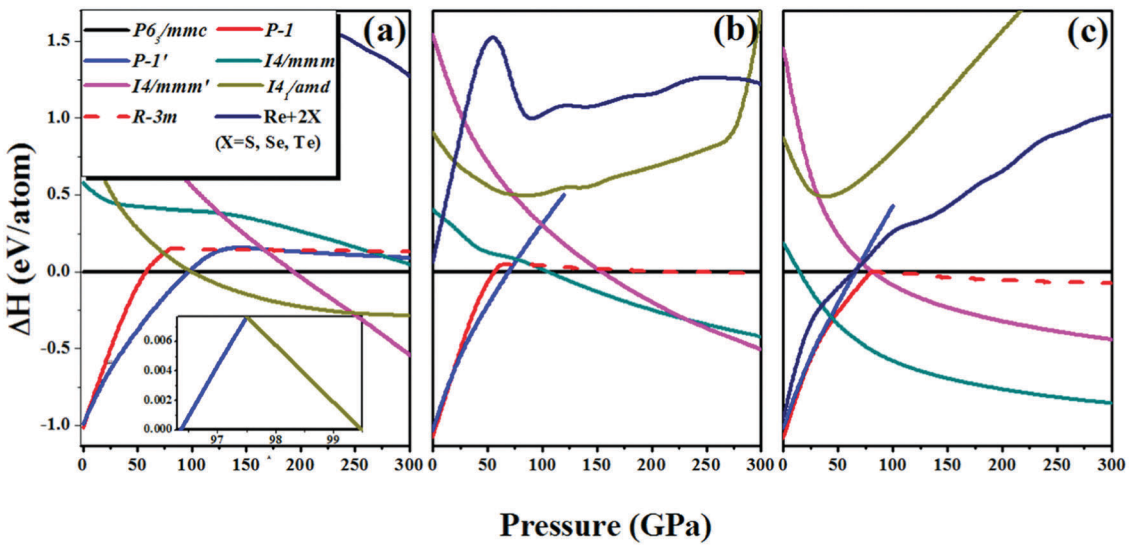


Fig. 1 The enthalpies (relative to the $P6_3/mmc$ structure) as a function of pressure of $ReS_2$ (a), $ReSe_2$ (b), and $ReTe_2$ (c). We adopt the hP2 structure of Re; the hP3 (Se-I) phase, the Se-III phase, the β-Po phase, the bcc phase, and the fcc phase of Se; the Te-I phase, the β-Po phase, the bcc phase, and the fcc phase of Te; the oF128 phase, the hP9 phase, the S-II phase and the $\beta$-Po phase of S as the reference phases in their own stable pressure ranges.

Table 1 Comparison of the calculated lattice parameters and volumes at 0 GPa using the GGA-PBE functional and the optB86b functional with vdW-DF correction with experimental values

| | $ReS_2$ ($P\bar{1}$) | | | $ReSe_2$ ($P\bar{1}$) | | | $ReTe_2$ ($P\bar{1}$) | | |
|---|---|---|---|---|---|---|---|---|---|
| | PBE | optB86b | Expt | PBE | optB86b | Expt | PBE | optB86b | Expt |
| $a$ (Å) | 6.396 | 6.364 | 6.352 | 6.648 | 6.616 | 6.597 | 7.259 | 7.219 | 7.180 |
| $b$ (Å) | 6.501 | 6.466 | 6.446 | 6.770 | 6.738 | 6.710 | 7.073 | 7.048 | 6.548 |
| $c$ (Å) | 13.489 | 12.724 | 12.779 | 7.197 | 6.728 | 6.721 | 7.839 | 7.369 | 7.512 |

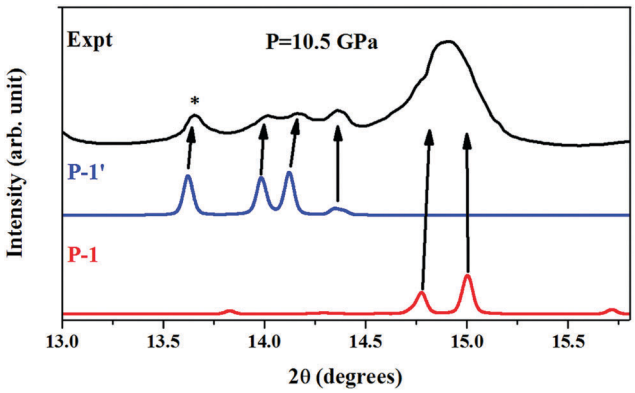


Fig. 2 Comparison of the experimental XRD data for $ReSe_2$ with a simulated XRD pattern for the ambient-pressure structure and the predicted $P\bar{1}'$ phase at 10.5 GPa. The XRD data from experiment at 10.5 GPa are shown as a black line and the simulated XRD curves of the $P\bar{1}$ phase and the $P\bar{1}'$ phase at 10.5 GPa are shown as blue and red lines, respectively. The peak marked with an asterisk is the new peak found in experiment.

vector $\vec{q}$, $\gamma_{\vec{q}j}$, resulting from electron–phonon interactions is as follows:

$$\gamma_{\vec{q}j} = 2\pi\omega_{\vec{q}j}\sum_{nm}\int\frac{d^3\vec{k}}{\Omega_{BZ}}\left|g^{j}_{\vec{k}n,\vec{k}+\vec{q}m}\right|^2\delta(\varepsilon_{\vec{k}n}-\varepsilon_F)\delta(\varepsilon_{\vec{k}+\vec{q}m}-\varepsilon_F), \quad (1.2)$$

where the sum is over the first BZ, with $\Omega_{BZ}$ as the volume of the BZ, $\varepsilon_{\vec{k}n}$ is the energy of the band measured relative to the Fermi level at point $\vec{k}$, and $g^{j}_{\vec{k}n,\vec{k}+\vec{q}m}$ represents the electron–phonon matrix element. The EPC parameter $\lambda$ can be expressed as:

$$\lambda = 2\int_0^\infty\frac{\alpha^2F(\omega)}{\omega}d\omega \approx \sum_{\vec{q}j}\lambda_{\vec{q}j}w(\vec{q}), \quad (1.3)$$

where $w(\vec{q})$ is the weight of a $\vec{q}$ point in the first BZ. Finally, the superconducting transition temperature $T_c$ can be estimated using the Allen–Dynes modified McMillan equation[35] as

$$T_c = \frac{\omega_{log}}{1.2}\exp\left[-\frac{1.04(1+\lambda)}{\lambda-\mu^*(1+0.62\lambda)}\right] \quad (1.4)$$

where $\omega_{log}$ is the logarithmic average frequency and $\mu^*$ is the Coulomb pseudopotential.

## Results and discussion

At ambient pressure, the experimentally-observed distorted-3R[13,14] phase (space group $P\bar{1}$) was accurately shown to be stable by our calculations. The interesting fact is that at high pressure, the $P\bar{1}$ phase transforms to the $R\bar{3}m$ phase after optimization as shown by a dashed line in Fig. 1, which is also a layer phase. The enthalpy curves of the candidate structures of $ReX_2$ relative to $P6_3/mmc$ are presented as a function of pressure in Fig. 1. All of the structural relaxations are based on the optB86b function together with the vdW-DF correction,[36] which minimize the errors compared to the calculation using GGA-PBE as shown in Table 1. A succession of phase transitions from $P\bar{1}$ (distorted-3R) → $P\bar{1}'$ (distorted-1T′) → $P6_3/mmc$ ($2H_c$) → $I4_1/amd$ → $I4/mmm'$ of $ReS_2$ was clearly revealed at 3.0 GPa, 96.5 GPa and 248.2 GPa respectively. The $P\bar{1}'$ phase and the $I4_1/amd$ phase in this work are consistent with earlier reports in Zhou *et al.*'s work.[17] Two new structures, $P6_3/mmc$ and $I4/mmm'$, were found to be mostly stable in the pressure range of 96.5–99.5 GPa and >248.2 GPa, respectively. $ReSe_2$ also shows a complex sequence of phase transitions from $P\bar{1}$ (distorted-3R) → $P\bar{1}'$ (distorted-1T′) → $P6_3/mmc$ ($2H_c$) → $I4/mmm$ → $I4/mmm'$ at 21.9 GPa, 69.2 GPa, 106 GPa and 231.7 GPa respectively. Fig. 2 shows a comparison of the experimental XRD[18]

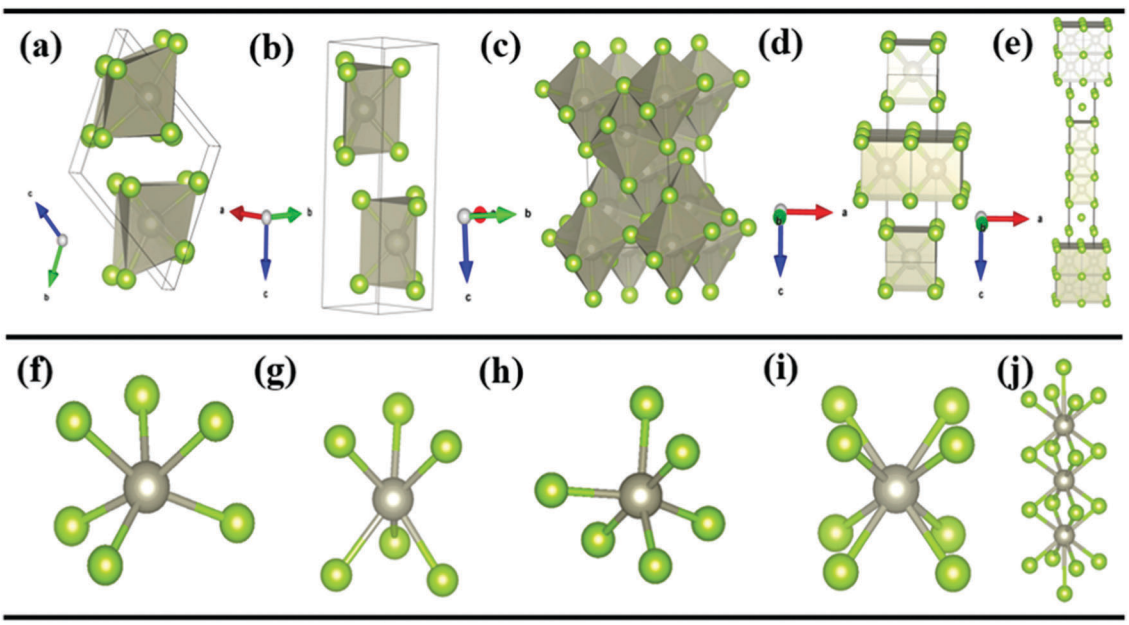


Fig. 3 The crystal structure of the $P\bar{1}'$ (a), $P6_3/mmc$ (b), $I4_1/amd$ (c), $I4/mmm$ (d) and $I4/mmm'$ (e) phases of $ReX_2$ and the local coordination environment of Re (f–j); the gray and green balls represent Re and X (X = S, Se, and Te) atoms, respectively.

 

patterns for $ReSe_2$ and the simulated XRD patterns of the ambient-pressure structure and the $P\bar{1}'$ phase predicted for 10.5 GPa. It can be seen that the peak marked with a star is a "fingerprint" of the new phase,[18] and the next three peaks in the experimental data are in good agreement with the XRD of $P\bar{1}'$ in our work as well. The strongest peak in the figure is from the $P\bar{1}$ phase for the sample that was dominated by the $P\bar{1}$ phase.[18] Therefore, our result demonstrates that the phase found by Kao *et al.* is indeed a distorted 1T′ phase with $P\bar{1}$ space group. In contrast to $ReS_2$ and $ReSe_2$, in $ReTe_2$, the ground state of the distorted-3R ($P\bar{1}$) structure directly transforms to a $I4/mmm$ phase at 50 GPa, which remains the lowest-enthalpy structure of $ReTe_2$ up to 300 GPa. All the high-pressure structures are stable against decomposition into elemental end-members as shown by the thermodynamic calculations (Fig. 1). The first-order phase transitions are indicated by the density increases across each transition, which are ~3%, ~1.9%, ~2.5% for $ReS_2$, ~15.2%, ~8.3% and ~1.3% for $ReSe_2$, and 4.7% for $ReTe_2$, respectively.

The high-pressure phases and corresponding unit cells of $ReX_2$ (X = S, Se, and Te) are depicted in Fig. 3, and the detailed structural information is shown in Table 3. The $P\bar{1}'$ phase (Fig. 3(a and f)) is a distorted-1T layer structure formed by a shear of the ground state distorted-3R structure. Within each layer, the Re atom is six-fold coordinated by X to form a $ReX_6$ octahedron. The $P6_3/mmc$ phase of $ReX_2$ (X = S and Se) corresponds to a $ReX_6$ triangular prism layer structure (Fig. 3(b and g)), which is a universal ground state in $TMX_2$ compounds.

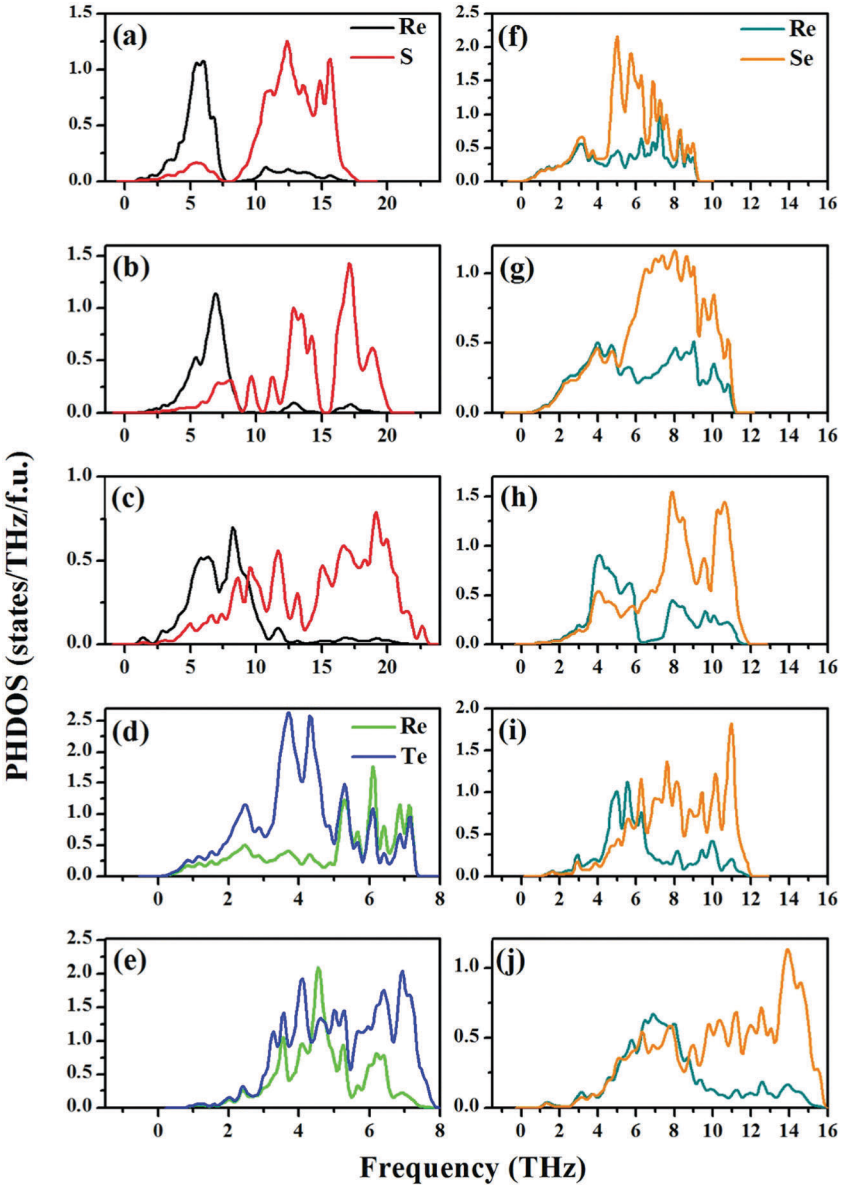


Fig. 4 The atom-projected PHDOSs of the $P6_3/mmc$ phase of $ReS_2$ at 97 GPa (a), the $I4_1/amd$ phase of $ReS_2$ at 100 GPa (b), the $I4/mmm'$ phase of $ReS_2$ at 300 GPa (c), the $P\bar{1}$ phase of $ReTe_2$ at 0 GPa (d), the $I4/mmm$ phase of $ReTe_2$ at 50 GPa (e), the $P\bar{1}$ phase of $ReSe_2$ at 0 GPa (f), the $P\bar{1}'$ phase of $ReSe_2$ at 40 GPa (g), the $P6_3/mmc$ phase of $ReSe_2$ at 100 GPa (h), the $I4/mmm$ phase of $ReSe_2$ at 150 GPa (i), and the $I4/mmm'$ phase of $ReSe_2$ at 300 GPa (j).

The $I4_1/amd$ phase (Fig. 3(c and h)) of $ReS_2$ was previously proposed by Zhou *et al.*[17] and is a close-stacking structure formed by $ReS_6$ edge-sharing irregular octahedra. The $I4/mmm$ structure (Fig. 3(d and i)) is composed of face-sharing $ReX_8$ cuboid layers, with adjacent layers displacing $a/2$ and $b/2$ along the $x$ and $y$ axes, respectively. The $I4/mmm'$ structure (Fig. 3(e and j)) consists of layers of close-packed $Re_3X_{18}$ units which can be considered as the stacking of three face-sharing $ReX_8$ cubes bonded *via* two X atoms along the $z$ axis. The adjacent layers are displaced $a/2$ and $b/2$ with respect to each other along the $x$ and $y$ axes. As expected from general pressure-coordination trends,[37] the coordination number of Re atom changes from 6 ($P\bar{1}'$, $P6_3/mmc$, and $I4_1/amd$) to 8 ($I4/mmm$ and $I4/mmm'$), and the coordination number of X by the X atom increases from 2 ($P\bar{1}$) to 3 ($P\bar{1}'$, $P6_3/mmc$, and $I4_1/amd$), and finally to 4 ($I4/mmm$ and $I4/mmm'$). With the increase of pressure, the Re–X distance is almost unchanged, but the X–X distance decreases significantly and becomes more comparable to the X–Re distance. This suggests that the X–X coordination environment might play an important role in determining the transition sequence. Indeed, it is found that the three phases with the X–X coordination number of 3 ($P\bar{1}'$, $P6_3/mmc$, and $I4_1/amd$) do not appear in the sequence of $ReTe_2$ and $I4_1/amd$ does not occur in $ReSe_2$. It seems that the X–X coordination number of 3 becomes much unfavorable with the increase of both the atomic radii of X and pressure.

In order to further explore and verify the structural stability of these structures, the phonon densities of states (PHDOSs) of all high-pressure phases of $ReX_2$ (X = S, Se, and Te) were calculated using the supercell method (Fig. 4). No imaginary phonon frequencies are found across the whole Brillouin zone, demonstrating the dynamical stability of these structures. Because pressure induces an increase in the force constants between atoms, the phonons of $ReX_2$ move to a higher frequency with increasing pressure.

The electronic band structure of $P\bar{1}'$ of $ReS_2$ at 60 GPa reveals its semi-conducting characteristics (Fig. 5). With the increase of pressure to 80 GPa, however, the bands already cross through the Fermi level and the material acts as a semimetal, with weak metallic properties. Our observations are in line with Zhou's work, which also found metallization in this phase at 70 GPa.[17] Similar metallization is also observed in the $P\bar{1}'$ phase of $ReSe_2$, which is a semiconductor at 40 GPa and a semimetal at 60 GPa. Naumov *et al.*[19] also described the metallization of $ReSe_2$ from resistivity curve analysis. For $ReTe_2$, the ground state of the $P\bar{1}$ phase becomes metallic below 10 GPa according to the bands shown in Fig. 5(e and f). It can be seen, therefore, that pressure induces metallization of $ReX_2$ (X = S, Se, and Te). For all the semimetal states of $ReX_2$ (X = S, Se, and Te), there are two bands through the Fermi level: one is an electron-like band, while the other is a hole-like band.

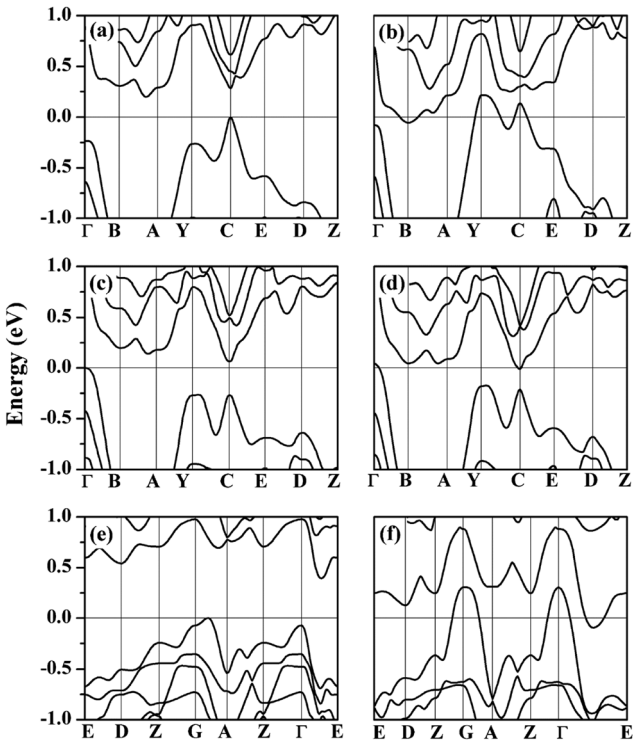


Fig. 5 The band structure of the $P\bar{1}'$ phase of $ReS_2$ at 40 GPa (a) and 80 GPa (b), the $P\bar{1}'$ phase of $ReSe_2$ at 40 GPa (c) and 60 GPa (d), and the $P\bar{1}$ phase of $ReTe_2$ at 0 GPa (e) and 10 GPa (f).

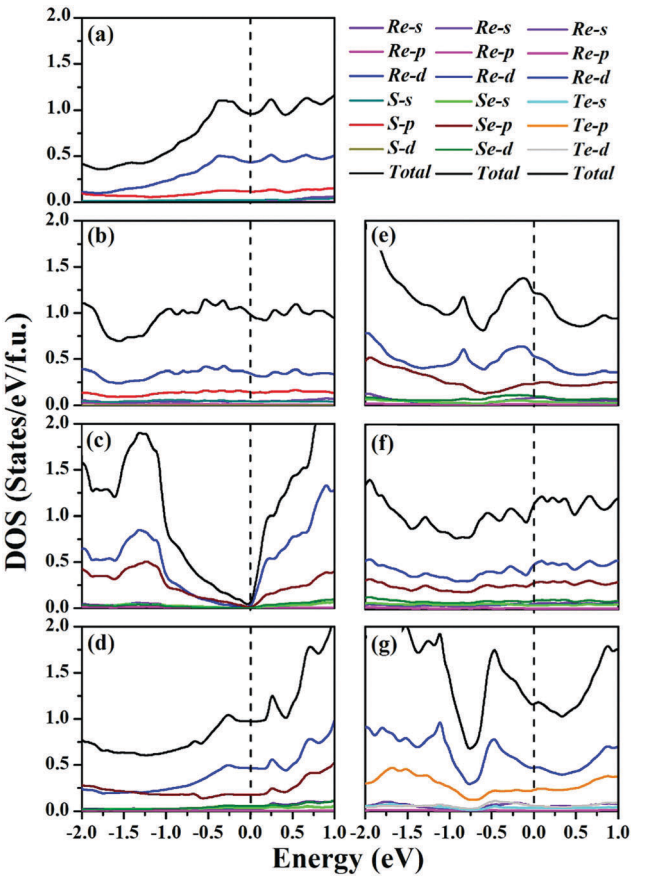


Fig. 6 The total and partial (or orbital-projected) DOSs of the $P6_3/mmc$ phase of $ReS_2$ at 97 GPa (a), the $I4/mmm'$ phase of $ReS_2$ at 300 GPa (b), the $P\bar{1}'$ phase of $ReSe_2$ at 40 GPa (c), the $P6_3/mmc$ phase of $ReSe_2$ at 100 GPa (d), the $I4/mmm$ phase of $ReSe_2$ at 150 GPa (e), the $I4/mmm'$ phase of $ReSe_2$ at 240 GPa (f), and the $I4/mmm'$ phase of $ReTe_2$ at 50 GPa (g).

 

According to the projected electronic densities of states (PDOSs), the $P\bar{1}'$ phases of $ReS_2$ and $ReSe_2$ are of poor metals. As expected, the total DOS at the Fermi level mainly comprises contributions from the Re 5d, S 3p, Se 4p, and Te 5p orbitals. Obvious hybridization occurs in the $P\bar{1}'$ and $P6_3/mmc$ phases of $ReSe_2$ (Fig. 6). Superconducting behavior has been extensively studied in transition metal dichalcogenides such as $WTe_2$, $TaS_2$, $NbSe_2$, $MoS_2$, $ReS_2$, among others.[4,6,17,38,39] From the band and DOS information, $ReX_2$ (X = S, Se, and Te) is metallic at high pressure. In addition, however, we have further studied the superconductivity of $ReSe_2$ and $ReTe_2$ below 200 GPa. We note that superconductivity in $ReS_2$ was reported previously by Zhou *et al.*,[17] therefore we have not repeated those calculations. The Eliashberg phonon spectral function $\alpha^2F(\omega)$, the logarithmic average phonon frequency $\omega_{log}$, and the electron–phonon coupling parameter $\lambda$ of the $P6_3/mmc$ structure of $ReSe_2$ at 100 GPa, the $I4/mmm$ structure of $ReSe_2$ at 150 GPa, and the $I4/mmm$ structure of $ReTe_2$ at 50 GPa are shown in Fig. 7. The resulting values of $\lambda$ are found to be 0.210, 0.238 and 0.245, respectively. $\mu^*$ is the Coulomb pseudopotential parameter and it remains challenging to directly derive an accurate $\mu^*$ from first-principles theory, but an upper bound on $\mu^*$ is estimated to be 0.25.[32] In the revision, we recalculated the superconducting transition temperatures ($T_c$) with a typical Coulomb pseudopotential parameter[40] $\mu^*$ = 0.13, and the $T_c$ of the $P6_3/mmc$ structure of $ReSe_2$ at 100 GPa, the $I4/mmm$ structure of $ReSe_2$ at 150 GPa, and the $I4/mmm$ structure of $ReTe_2$ at 50 GPa are 1.0 K, 2.0 K and 1.4 K, respectively. From the PHDOS, the Eliashberg EPC spectral function $\alpha^2F(\omega)$ and the electron–phonon integral $\lambda(\omega)$ (Fig. 7), it is evident that for the $P6_3/mmc$ phase of $ReSe_2$, the low-frequency translational vibrations from Se and Re atoms contribute similarly to $\lambda$ and the high-frequency translational vibrations from Se make more contribution than high-frequency translational vibrations from Re to $\lambda$ and the same tendency was also found in the $I4/mmm$ phase of $ReSe_2$. In the $I4/mmm$ phase of $ReTe_2$, Te atom vibrations make more contribution than Re atom vibrations to the overall EPC constant. We have added these analyses in the revision.

We have used crystal orbital Hamilton population (COHP) analysis to determine the strength and nature of the chemical bonding of Re–X (X = S, Se, and Te) pairs in all high-pressure phases. The averaged COHP of Re–X (X = S, Se, and Te) atom pairs are shown in Fig. 8. The negative value (low energy region) of the COHP indicates any bonding character between such Re–X (X = S, Se, and Te) pairs. The integrated crystal orbital

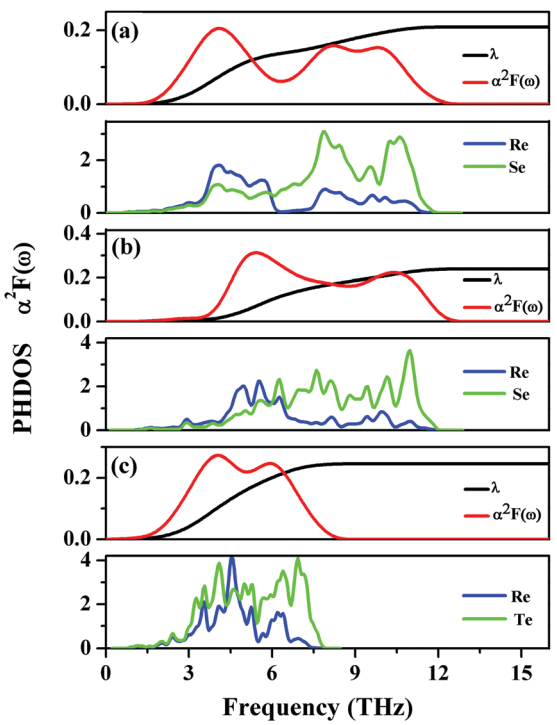


Fig. 7 The calculated projected phonon density of states (lower panels), the Eliashberg EPC spectral function $\alpha^2F(\omega)$ and its integral $\lambda(\omega)$ (upper panels) of (a) the $P6_3/mmc$ phase of $ReSe_2$ at 100 GPa, (b) the $I4/mmm$ phase of $ReSe_2$ at 150 GPa and (c) the $I4/mmm$ phase of $ReTe_2$ at 50 GPa.

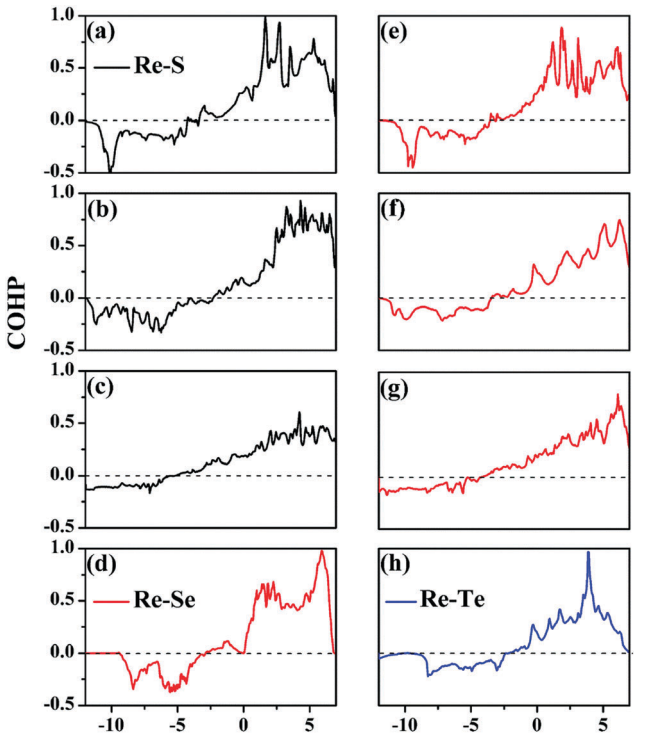


Fig. 8 The COHP of Re–S pairs for the $P6_3/mmc$ structure at 97 GPa (a), $I4_1/amd$ at 100 GPa (b), $I4/mmm'$ at 300 GPa (c); Re–Se pairs in the $P\bar{1}'$ phase at 40 GPa (d), $P6_3/mmc$ at 100 GPa (e), $I4/mmm$ at 150 GPa (f), $I4/mmm'$ at 240 GPa (g) and Re–Te pairs in the $I4/mmm$ phase at 50 GPa (h). The Fermi level is at the energy origin.

Table 2 ICOHP values of new predicted phases of $ReS_2$, $ReSe_2$ and $ReTe_2$

| ICOHP phase | $ReS_2$ (Re–S) | $ReSe_2$ (Re–Se) |
|---|---|---|
| $P\bar{1}'$ | — | −3.54 (40 GPa) |
| $P6_3/mmc$ | −3.48 (97 GPa) | −3.33 (100 GPa) |
| $I4_1/amd$ | −3.74 (100 GPa) | — |
| $I4/mmm$ | — | −2.97 (150 GPa) |
| $I4/mmm'$ | −2.70 (300 GPa) | −1.34 (240 GPa) |
| | −2.78 (300 GPa) | −2.81 (240 GPa) |

Table 3 Structural information of new phases of $ReS_2$, $ReSe_2$ and $ReTe_2$

| Systems | Pressure | Space group | Lattice parameter (Å, °) | Atom | Atomic coordinates (fractional) $x$ | $y$ | $z$ |
|---|---|---|---|---|---|---|---|
| $ReS_2$ | 97 GPa | $P6_3/mmc$ | $a = b = 2.734$, $c = 10.128$ | Re(2d) | 0.667 | 0.333 | 0.250 |
| | | | $\alpha = \beta = 90$, $\gamma = 120$ | S(4f) | 0.667 | 0.333 | 0.913 |
| | 140 GPa | $I4_1/amd$ | $a = b = 4.230$, $c = 6.698$ | Re(4a) | 1 | −0.5 | 0.75 |
| | | | | S(8e) | 0.5 | 0 | 0.587 |
| | 300 GPa | $I4/mmm'$ | $a = b = 2.560$, $c = 22.376$ | Re(4e) | 0 | 0 | 0.5 |
| | | | $\alpha = \beta = \gamma = 90$ | Re(4e) | 0.5 | 0.5 | 0.116 |
| | | | | S(4e) | 0.5 | 0.5 | 0.325 |
| | | | | S(4e) | 0.5 | 0.5 | 0.442 |
| | | | | S(4e) | 0 | 0 | 0.277 |
| $ReSe_2$ | 40 GPa | $P\bar{1}'$ | $a = 6.341$, $b = 6.081$, $c = 6.066$ | Se(2i) | 0.182 | 0.746 | 0.57 |
| | | | $\alpha = 116.340$, $\beta = 75.508$, $\gamma = 75.219$ | Se(2i) | 0.370 | 0.218 | 0.359 |
| | | | | Se(2i) | 0.693 | 0.280 | 0.013 |
| | | | | Se(2i) | 0.142 | 0.301 | 0.066 |
| | | | | Re(2i) | 0.487 | 0.220 | 0.708 |
| | | | | Re(2i) | 0.933 | 0.806 | 0.331 |
| | 80 GPa | $P6_3/mmc$ | $a = b = 2.832$, $c = 11.286$ | Re(2d) | 0.667 | 0.333 | 0.25 |
| | | | $\alpha = \beta = 90$, $\gamma = 120$ | Se(4f) | 0.667 | 0.333 | 0.907 |
| | 120 GPa | $I4/mmm$ | $a = b = 2.707$, $c = 9.7406$ | Re(2b) | 0 | 0 | 0.5 |
| | | | $\alpha = \beta = \gamma = 90$ | Se(4e) | 0.50 | 0.5 | 0.845 |
| | 240 GPa | $I4/mmm'$ | $a = b = 2.681$, $c = 25.324$ | Re(2a) | 0 | 0 | 0 |
| | | | $\alpha = \beta = \gamma = 90$ | Re(4e) | 0 | 0 | 0.109 |
| | | | | Se(4e) | 0.5 | 0.5 | 0.173 |
| | | | | Se(4e) | 0.5 | 0.5 | 0.196 |
| | | | | Se(4e) | 0 | 0 | 0.663 |
| $ReTe_2$ | 60 GPa | $I4/mmm$ | $a = b = 2.976$, $c = 11.000$ | Re(2b) | 0 | 0 | 0.50 |
| | | | $\alpha = \beta = \gamma = 90$ | Te(4e) | 0.5 | 0.5 | 0.352 |

Hamilton population (ICOHP) was calculated to analyze the strength and nature of chemical bonding between Re atoms and X (S, Se, and Te) atoms, as shown in Table 2. For $ReS_2$, the Re–S bonds in the $P6_3/mmc$ structure (−3.48) are stronger than the Re–S bonds in the $I4/mmm'$ structure (−2.74) but similar to those in the $I4_1/amd$ (−3.74) phase. The ICOHP values of Re–Se bonds of the $P\bar{1}'$ (−3.54) and $P6_3/mmc$ (−3.33) phases of $ReSe_2$ are also similar, however they are all smaller than the ICOHP of $I4/mmm$ (−2.97) and $I4/mmm'$(−2.08) $ReSe_2$, indicating that the Re–Se bonds in the $P\bar{1}'$ and $P6_3/mmc$ phases are stronger than those in the $I4/mmm'$ phase of $ReSe_2$. Similarly, the Re–Te bonds of six-fold coordinated Re in $P\bar{1}'$ $ReTe_2$ are stronger than the Re–Te bonds in the $I4/mmm$ phase, as revealed by the ICOHP of $P\bar{1}$ (−3.12) $ReTe_2$ being larger than that of the $I4/mmm$ (−2.22) phase.

## Conclusions

In summary, we have investigated the high-pressure behavior of the transition metal dichalcogenide $ReX_2$ system. Five high-pressure phases, $P\bar{1}'$, $P6_3/mmc$, $I4_1/amd$, $I4/mmm$ and $I4/mmm'$, were predicted in the $ReX_2$ family of compounds and are found to be energetically stable over certain pressure ranges. Thermodynamical calculations revealed that all the high-pressure phases of $ReX_2$ are stable with respect to elemental decomposition at least up to 300 GPa. With the increase of pressure, the coordinated environment changes from a $ReX_6$ octahedron or a trigonal prism to a $ReX_8$ cuboid. Moreover, our electron–phonon coupling calculations have revealed the superconducting potential of metallic $ReX_2$ phases. Our simulated X-ray diffraction patterns, from our computed structures for $ReSe_2$, are in good agreement with previous experimental data.

## Conflicts of interest

The authors declare no competing financial interest.

## Acknowledgements

This work was supported by NSAF No. U1530124; the National Natural Science Foundation of China under Grants No. 11474128, 11774127, 11534003 and 11764043; the National Key Research and Development Program of China under Grant No. 2016YFB0201200, 2016YFB0201201, and 2017YFB0701503; the 2012 Changjiang Scholars Program of China supported by the Program for JLU Science and Technology Innovative Research Team; the Science Challenge Project No. TZ2016001 and the NSF-CREST Center for Innovation, Research and Education in Environmental Nanotechnology with Grant Number HRD-1736093 and NASA with Grant 17-EPSCoRProp-0032.

 

## References


1 M. Marezio, P. Dernier, A. Menth and G. Hull Jr, *J. Solid State Chem.*, 1972, **4**, 425–429.
2 C. Fang, G. Wiegers, C. Haas and R. De Groot, *J. Phys.: Condens. Matter*, 1997, **9**, 4411.
3 M. Chhowalla, H. S. Shin, G. Eda, L.-J. Li, K. P. Loh and H. Zhang, *Nat. Chem.*, 2013, **5**, 263.
4 P. Lu, J.-S. Kim, J. Yang, H. Gao, J. Wu, D. Shao, B. Li, D. Zhou, J. Sun and D. Akinwande, *Phys. Rev. B*, 2016, **94**, 224512.
5 B. E. Brown, *Acta Crystallogr.*, 1966, **20**, 268–274.
6 O. Kohulák and R. Martoňák, *Phys. Rev. B*, 2017, **95**, 054105.
7 X. Wang, X. Chen, Y. Zhou, C. Park, C. An, Y. Zhou, R. Zhang, C. Gu, W. Yang and Z. Yang, *Sci. Rep.*, 2017, **7**, 46694.
8 H. S. Broadbent, L. H. Slaugh and N. L. Jarvis, *J. Am. Chem. Soc.*, 1954, **76**, 1519–1523.
9 B. L. Wheeler, J. K. Leland and A. J. Bard, *J. Electrochem. Soc.*, 1986, **133**, 358–361.
10 F.-P. Koffyberg, K. Dwight and A. Wold, *Solid State Commun.*, 1979, **30**, 433–437.
11 Y.-C. Lin, H.-P. Komsa, C.-H. Yeh, T. Bjorkman, Z.-Y. Liang, C.-H. Ho, Y.-S. Huang, P.-W. Chiu, A. V. Krasheninnikov and K. Suenaga, *ACS Nano*, 2015, **9**, 11249–11257.
12 B. Jariwala, A. Thamizhavel and A. Bhattacharya, *J. Phys. D: Appl. Phys.*, 2016, **50**, 044001.
13 V. Larchev and S. Popova, *Inorg. Mater.*, 1976, **12**, 1130–1132.
14 H.-J. Lamfers, A. Meetsma, G. Wiegers and J. De Boer, *J. Alloys Compd.*, 1996, **241**, 34–39.
15 L. Zhang, Y. Wang, J. Lv and Y. Ma, *Nat. Rev. Mater.*, 2017, **2**, 17005.
16 D. Hou, Y. Ma, J. Du, J. Yan, C. Ji and H. Zhu, *J. Phys. Chem. Solids*, 2010, **71**, 1571–1575.
17 D. Zhou, Y. Zhou, C. Pu, X. Chen, P. Lu, X. Wang, C. An, Y. Zhou, F. Miao and C.-H. Ho, *npj Quantum Mater.*, 2017, **2**, 19.
18 Y.-C. Kao, T. Huang, D.-Y. Lin, Y.-S. Huang, K.-K. Tiong, H.-Y. Lee, J.-M. Lin, H.-S. Sheu and C.-M. Lin, *J. Chem. Phys.*, 2012, **137**, 024509.
19 P. Naumov, M. ElGhazali, H. Mirhosseini, V. Süß, E. Morosan, C. Felser and S. Medvedev, *J. Phys.: Condens. Matter*, 2017, **30**, 035401.
20 Y. Wang, J. Lv, L. Zhu and Y. Ma, *Phys. Rev. B: Condens. Matter Mater. Phys.*, 2010, **82**, 094116.
21 Y. Wang, J. Lv, L. Zhu and Y. Ma, *Comput. Phys. Commun.*, 2012, **183**, 2063–2070.
22 H. Wang, S. T. John, K. Tanaka, T. Iitaka and Y. Ma, *Proc. Natl. Acad. Sci. U. S. A.*, 2012, **109**, 6463–6466.
23 H. Liu, I. I. Naumov, R. Hoffmann, N. Ashcroft and R. J. Hemley, *Proc. Natl. Acad. Sci. U. S. A.*, 2017, **114**, 6990–6995.
24 J. P. Perdew, J. A. Chevary, S. H. Vosko, K. A. Jackson, M. R. Pederson, D. J. Singh and C. Fiolhais, *Phys. Rev. B: Condens. Matter Mater. Phys.*, 1992, **46**, 6671.
25 J. P. Perdew, K. Burke and M. Ernzerhof, *Phys. Rev. Lett.*, 1996, **77**, 3865.
26 G. Kresse and J. Furthmüller, *Phys. Rev. B: Condens. Matter Mater. Phys.*, 1996, **54**, 11169.
27 P. E. Blöchl, *Phys. Rev. B: Condens. Matter Mater. Phys.*, 1994, **50**, 17953.
28 H. J. Monkhorst and J. D. Pack, *Phys. Rev. B: Condens. Matter Mater. Phys.*, 1976, **13**, 5188.
29 A. Togo, F. Oba and I. Tanaka, *Phys. Rev. B: Condens. Matter Mater. Phys.*, 2008, **78**, 134106.
30 P. Giannozzi, S. Baroni, N. Bonini, M. Calandra, R. Car, C. Cavazzoni, D. Ceresoli, G. L. Chiarotti, M. Cococcioni and I. Dabo, *J. Phys.: Condens. Matter*, 2009, **21**, 395502.
31 S. Maintz, V. L. Deringer, A. L. Tchougréeff and R. Dronskowski, *Chem.*, 2016, **37**, 1030–1035.
32 P. B. Allen and R. Silberglitt, *Phys. Rev. B: Condens. Matter Mater. Phys.*, 1974, **9**, 4733.
33 P. B. Allen, *Phys. Rev. B: Condens. Matter Mater. Phys.*, 1972, **6**, 2577.
34 J. Bardeen, L. N. Cooper and J. R. Schrieffer, *Phys. Rev.*, 1957, **108**, 1175.
35 P. B. Allen and R. Dynes, *Phys. Rev. B: Condens. Matter Mater. Phys.*, 1975, **12**, 905.
36 M. Dion, H. Rydberg, E. Schröder, D. C. Langreth and B. I. Lundqvist, *Phys. Rev. Lett.*, 2004, **92**, 246401.
37 G. Gao, R. Hoffmann, N. W. Ashcroft, H. Liu, A. Bergara and Y. Ma, *Phys. Rev. B: Condens. Matter Mater. Phys.*, 2013, **88**, 184104.
38 E. Boaknin, M. Tanatar, J. Paglione, D. Hawthorn, F. Ronning, R. Hill, M. Sutherland, L. Taillefer, J. Sonier and S. Hayden, *Phys. Rev. Lett.*, 2003, **90**, 117003.
39 B. Sipos, A. F. Kusmartseva, A. Akrap, H. Berger, L. Forró and E. Tutiš, *Nat. Mater.*, 2008, **7**, 960.
40 F. Peng, Y. Sun, C. J. Pickard, R. J. Needs, Q. Wu and Y. Ma, *Phys. Rev. Lett.*, 2017, **119**(10), 107001.